JOURNAL OF MATERIALS SCIENCE 20 (1985) 4624–4646

An investigation of ion implantation-induced near-surface stresses and their effects in sapphire and glass

P. J. BURNETT*, T. F. PAGE
Department of Metallurgy and Materials Science, University of Cambridge, Pembroke Street, Cambridge, UK

Using both cantilever bending and indentation fracture techniques, the generation of near-surface compressive stresses by ion-implantation into sapphire and glass has been monitored and characterized. In all cases, the surface stresses initially increase with ion dose until a critical dose (dependent on material and ion species/energy) is reached. Beyond this dose, stress relief has been observed and, for sapphire implanted with both Y^+ and Ti^+, this has been attributed to the formation and growth of an amorphous layer as monitored by hardness testing. The stress relief has been simply modelled and values estimated for the mechanical strength of the amorphous layer produced. For sapphire, the integrated stress produced over the near-surface volume was found to increase linearly with dose; values of the integrated stress produced by the two different species were similar when considered in terms of energy deposition. Estimates of the contribution to the integrated stress of both the implantation-induced damage and the implanted species profile suggest that the implanted profile makes a minor but significant ($\lesssim 20\%$) contribution. Broadly similar behaviour was observed for soda-lime–silica glass specimens implanted with both C^+ and N^+. While the origins of the compressive stress produced are probably similar to those in crystalline materials (i.e. defect production and ion-stuffing), no microstructural explanations for both the observed hardening with increasing dose and stress relief have been forthcoming. However, high-dose implantation of N^+ into glass leads to blistering and concomitant softening.

1. Introduction

Recent work has shown that ion implantation into brittle materials may be a viable process for modifying those near-surface mechanical properties important in wear-related processes (e.g. hardness and indentation fracture), together with the possible changes in the sensitivity of certain materials to environmental attack. A range of such implantation-induced effects have been reported by ourselves and others for various substrates [1–5]. For example, hardening may be induced at doses of $\sim 10^{16}$ ions cm^{-2} in Al_2O_3, whilst surface softening related to amorphization is observed at higher doses (typically $\sim 10^{17}$ ions cm^{-2}). In some cases, precipitation-hardening effects may also be induced by post-implantation heat treatment (e.g. [2, 3]). In addition, it is known that ion implantation can

**Present address*: Department of Metallurgy and Science of Materials, University of Oxford, Parks Road, Oxford, UK.

0022–2461/85 $03.00 + .12 © *1985 Chapman and Hall Ltd.*

induce high levels of stress in the surface. This stress has been shown to be compressive for most ion-target combinations (e.g. [6, 7]), although it is known that tensile stresses may be produced by implantation of light ions (e.g. H^+, He^+) into amorphous targets such as vitreous silica (e.g. [8, 9]). Using cantilever bending techniques, Krefft and Eernisse [6] have also shown that light-ion implantation into sapphire, previously implanted with heavy ions, may relieve the compressive stresses resulting from this heavy-ion implantation. Compressive stresses are usually attributed to extensive defect production, together with the "ion stuffing" effect of the implanted species. The tensile stresses from light-ion implantation are thought to result from possible structural compaction/relaxation processes (e.g. [8, 9]). While the depth of material modified by even highly energetic implantation processes is thin (typically $\sim 0.5\,\mu m$), the biaxial compressive stresses produced in this layer can be of the order of 1 to 10 GPa.

The possible effects of implantation-induced stresses in modifying surface behaviour are potentially important and could involve changes to crack nucleation, crack growth and plasticity mechanisms. However, the action of the implantation-induced stress state upon the indentation-fracture response of brittle materials is only just beginning to be understood (e.g. [10]). The extent of the previous observations made by us and other workers are: (a) that the compressive stresses may cause an apparent increase in indentation fracture toughness (K_c) resulting from the increased difficulty in propagating a median/radial crack through the compressed surface layer (e.g. [4, 5, 10]), and (b) the suppression and/or reduction of lateral crack formation under both static and sliding point contacts (e.g. [10, 11]).

In a recent paper, Lawn and Fuller [12] have proposed a quantitative model relating changes in the extent of radial cracks to the presence of a thin, highly-stressed surface layer. They found good agreement with results of experiments inducing tensile stresses into amorphous silica by light-ion implantation [13].

The studies described in the present paper have been designed to explore more fully both the generation of surface stresses during the implantation of brittle materials and their effects on surface mechanical response. The aims have been:

(i) to correlate stress levels with both dose and, more importantly, the related structural changes occurring as a result of cumulative damage;

(ii) to experimentally quantify the stress levels using the observed effects on crack propagation (using the Lawn and Fuller model) together with the cantilever bending technique described by Eernisse; and

(iii) to develop a simple model for the level of surface stress in terms of the expected properties of the changing surface microstructure with particular reference to the stress-relief accompanying surface amorphization.

Experiments have been performed with single-crystal sapphire and soda-lime–silica glass specimens implanted with Ti^+, Y^+, and C^+, N^+ respectively to doses in the range 10^{15} to 10^{18} ions cm^{-2}. The variations of hardness and indentation fracture toughness with ion-dose were determined and the surface structural state inferred from the hardness response as described in our previous work [1–3]. Besides exploring the objectives stated above, the yield stress of the amorphized sapphire was also estimated.

2. Ion implantation-induced modifications to microstructure and stress state

Ion implantation is a low-temperature vacuum surface treatment process involving ion-energies typically in the range 50 to 500 keV. Energetic ions penetrate the surface of the target (host) material and come to rest in an approximately Gaussian distribution (e.g. [14]). Various theoretical models have been devised to predict the ion ranges for any particular ion/energy/target combination, the most commonly used (and, indeed, the model used here) being that due to Lindhard *et al.* (LSS) [15].

The implanted ions lose energy by two mechanisms prior to coming to rest. Firstly, inelastic collisions result in the displacement of host atoms from their structure-sites. These displaced atoms may then proceed to displace other host atoms until, finally, the energies of both the incident ions and the recoiling host atoms are insufficient to produce further displacements. For most materials the energy needed to displace

an atom from its structure-site is $\sim 25\,\mathrm{eV}$ [14], and thus the number of displacements per incident ion is expected to be large.

Secondly, fast-moving ions may lose energy by electronic excitation of the host material. This can result in the weakening of the host atom bonding by ionization and the formation of charged defects such as colour centres (e.g. [16]). Such processes are more efficient at higher ion energies with displacements prevalent at lower energies, the competition between the processes (combined with the statistical nature of the collision processes) producing the typically Gaussian damage and concentration profiles usually assumed. Again, theoretical models predicting both the energy partitioning between the collisional and electronic energy loss processes and the spatial distribution of the resultant damage patterns have been developed (e.g. [17]). The model and computer code EDEP–1 due to Manning and Mueller has been used in this study [18]. This model produces values for the energy partitioning between displacement and electronic excitation damage mechanisms, together with predicted profiles for both the distribution of damage and ion species (using the LSS theory). While the model actually predicts a deviation from Gaussian behaviour for both the damage and concentration profiles, the curves being skewed to higher than Gaussian values near the surface, simple Gaussian behaviour has been assumed throughout this work for ease of later modelling and computation.

As implantation proceeds, the accumulation of displacement damage may lead to the host material (if crystalline) eventually becoming amorphous [14]. This has been observed by a number of workers for a wide range of both covalently-bonded and ionically-bonded materials (e.g. silicon [1, 11], SiC [4], Al_2O_3 [2] and MgO [3]). Typically, it is estimated that between 0.1 and 1.0 displacements per host atoms (DPA) need to occur for amorphization. However, in practice, the target atoms may be displaced many more times than this prior to amorphization since some amount of both radiation- and thermal-annealing occurs. Such *in situ* self-annealing appears to occur more readily in ionically-bonded than covalently-bonded materials, and thus amorphization occurs at lower doses (or more correctly, lower energy deposition levels) in covalent solids than

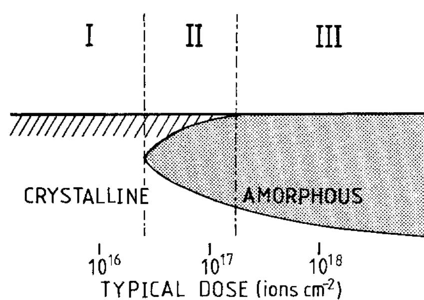

Figure 1 A schematic representation of the three microstructural regimes that may arise from ion-implantation into crystalline materials. In Region I, at low dose (or specifically, low energy deposition — see text), a damaged but still crystalline solid solution is formed. In Region II, at intermediate doses, amorphous material is initially formed at the peak of the displacement damage profile, resulting in a sub-surface amorphous layer which thickens with increasing dose. In Region III, at sufficiently high doses, a true surface amorphous layer is formed which also thickens with increasing dose. In reality, the transitions from crystalline to damaged to amorphous regions may well be much more gradual than the diagram suggests.

in ionic solids. Amorphization is expected to occur first at the peak of the displacement damage profile beneath the host surface, i.e. initially a sub-surface amorphous zone occurs once the damage peak exceeds some critical, material-dependent, value. The thickness of this zone increases with subsequent increases in dose, until, when the damage level at the surface exceeds the critical value, a surface amorphous layer will be formed. Consequently it can be seen that, as the implantation dose is increased, three distinct microstructural regimes occur; these are summarized in Fig. 1.

Finally, the generation of the point defects by displacement processes results in a volume change within the implanted layer. Volume expansions of up to 30% have been reported (e.g. [4]). However, if this change is constrained by either underlying or surrounding material, as is usual, large stresses may be generated in this relatively thin implanted layer (e.g. [6]). As mentioned in Section 1, both compressive and tensile stresses have been observed depending upon the nature of the host material and ion species.

3. Experimental procedure
3.1. Ion implantation
High-purity semiconductor substrate single-

TABLE I Implantation conditions

Material	Ion species and energy	Dose range (ions cm^{-2})	Range parameters (μm)		Damage parameters (μm)		Displacement damage energy (keV per ion)*
			R_p [‡]	ΔR_p	$\langle X_D \rangle$	$\langle \Delta X_D \rangle$	
Sapphire	Ti^+ 300 keV	3×10^{16} to 5×10^{17}	0.143	0.0407	0.088	0.0508	125
	Y^+ (300 keV	1×10^{16} to 5×10^{17}	0.081	0.0234	0.046	0.0282	152
Soda-lime–silica glass	C^+ 100 keV	1×10^{16} to 5×10^{17}	0.25	0.070	0.16	0.090	25
	N^+ 45 keV	5×10^{19} to 5×10^{17}	0.13	0.043	0.0800	0.048	~19
	N^+ 90 keV		0.26	0.086	0.160	0.096	

*Pimento implant; see text for actual beam composition.
[†] Calculated using the EDEP–1 computer code [18].
[‡] Defined in [1, 10].

crystal sapphire wafers (~75 mm × 0.4 mm) of $\{10\bar{1}2\}$ surface were supplied with one side pre-polished to a good finish (by courtesy of GEC Ltd, Wembley). These were subsequently cleaved and/or cut (using a Capco high-speed annular diamond saw) to sections of size 5 mm × 20 mm × 0.4 mm. These sections were mounted with silver paint, at one end only, on to sections of glass microscope slides or metal discs. The mounting was such that most of the specimen length was raised clear to the slide, so that the unfixed end of the sapphire would be free to deflect in response to the stresses induced by implantation. The whole specimen surfaces were then implanted with either Ti^+ or Y^+ (both at 300 keV) in the Cockcroft–Walton facility at the Atomic Energy Research Establishment, Harwell. The ion doses were subsequently determined using Rutherford back-scattering analysis [1, 14]. Mid-mass range species were chosen to provide a reasonable compromise in damage and range. The glass specimens were commercial soda-lime–silica microscope slides. These were ultrasonically cleaned prior to implantation with either C^+ at 100 keV (in the Cockcroft–Walton) or N_2^+ at 90 keV (in the "Pimento" at AERE Harwell)*. These specimens were chosen to enable comparison with previous work [19, 20]. The doses of N_2^+ into glass were subsequently checked using nuclear reaction analysis (d, α [21]).

The implantation conditions for both sapphire and glass are summarized in Table I. The Gaussian range, damage parameters and energy partitioning data (as evaluated using the Harwell version of the EDEP–1 computer code [22]) are also presented.

3.2. Indentation techniques

Both Knoop and Vickers profile diamond indenters were used to determine the indentation response (both hardness and indentation fracture) of the specimens. For all cases, a Leitz "Mini-load" microhardness testing machine was utilized under ambient laboratory conditions. A constant loading cycle time of 15 sec was used for all tests in order to minimize errors that could be introduced by indentation creep. Subsequent measurements were made under constant lighting conditions in a darkened room.

For sapphire, Knoop indentations at loads of 25 and 50 g were used to determine the variation in hardness of the near-surface implanted layer (as previously described by us [2, 3]). The indentation long diagonal lengths were typically in the range 10 to 15 μm corresponding to indenter penetrations of ~0.3 to 0.5 μm. These depths are comparable to the thickness of the implanted layer, and thus the hardness values obtained reflect substantially the hardness of the implanted layer. The long diagonal of the indenter was always aligned along one of the $\langle 0\bar{2}21 \rangle$ directions in the surface to minimize the effect of hardness anisotropy. For glass, Knoop indentations of 10 and 25 g were used and the same considerations concerning indenter penetration and implanted layer thickness apply as for sapphire above. No special alignment of the indenter was necessary.

In all cases, typically six indentations per

*The Pimento accelerator yields an unfiltered beam at ~75% N_2^+ at 90 keV, the balance being N^+ at 90 keV. The N_2^+ ions are assumed to split, on contact with the surface, into 2 × N^+ at 45 keV, thus the actual dose of N^+ will be 7/4 times the "stated dose" of N_2^+ (~16% of which is at 90 keV, the balance being at 45 keV).

specimen were measured and the hardness determined from the mean of the diagonals. After indentation, and prior to measurement, all specimens were lightly gold-coated to increase the reflectivity of the surface.

Vickers indentations of loads of 100 to 500 g were used to induce the well-known lateral/median/radial indentation fracture patterns described by Lawn and co-workers (e.g. [23]). Indentation diagonals and radial crack trace lengths were measured (without gold coating). For the sake of consistency, only the well-formed $\langle 0\bar{2}21 \rangle$ traces of the two $\{\bar{1}102\}$ cracks (at $\sim 90°$ to each other) on the sapphire surface were measured since the other crack system present, the $(1\bar{2}10)$ plane, would probably possess a different work of fracture, thus clouding any effect upon crack propagation that ion implantation can induce. (Burnett and Page [10] gives a detailed description of these crack geometries.) All well-developed cracks were measured in the glass. On average, 30 cracks per load were measured for each specimen. For all the indentation fracture experiments the indenter penetration exceeded the implanted layer depth by a factor of $\gtrsim 10$.

Scanning electron microscopy (SEM) and reflected light microscopy (including polarizing techniques) were used to study the deformation and fracture around the indentations.

3.3. Cantilever bending

The surface curvatures produced by the action of implantation-induced surface stresses upon the relatively thin sapphire specimens were determined by careful use of a "Talysurf 10" surface profilometer. Several passes were made along the $\langle 0\bar{2}21 \rangle$ direction parallel to the longest dimension of the specimens. The central 10 to 15 mm of each specimen was measured. The deflections of the specimens over this length were determined and the integrated stress calculated according to the method of Eernisse [6, 8] (see Section 4.2). Prior to profilometry, the specimens were removed from the glass mounts used for the implantation process and ultrasonically cleaned. In order to improve specimen rigidity during profilometry they were then re-mounted by dropping on to a "puddle" of silver paint on another microscope slide, care being taken not to stress the sapphire pieces during this process.

4. Results and interpretation

4.1. Hardening behaviour

The hardness variations of $\{10\bar{1}2\}$ sapphire with dose for implantation of Ti^+ and Y^+ at 300 keV are shown in Figs. 2 and 3. The observed behaviour is essentially similar to that previously reported both by ourselves [2, 10] and by other workers [24, 25]. For both implant species, hardness increases are apparent in the lower-dose specimens. Peak hardness values were observed at doses of $\sim 8 \times 10^{16}\ Ti^+\ cm^{-2}$ and $\sim 2 \times 10^{16}\ Y^+\ cm^{-2}$ respectively, softening occurring beyond these doses. Eventually, at doses typically $\gtrsim 10^{17}$ ions cm^{-2}, a surface softer than that of the original host materials was observed (absolute softening). Our earlier studies have clearly correlated this progressive softening with the evolution of an amorphous layer [1–3]. Adopting the nomenclature used in our previous work (and in Figs. 1 to 3), "Region I" behaviour (i.e. hardness increasing with dose) corresponds to the presence of a radiation-damaged, but still crystalline implanted layer. Hardening is attributed principally to radiation hardening effects though there may be some contribution from solid-solution hardening, i.e. ion-misfit and/or electrostatic (charge compensation) effects with aliovalent ions such as Ti^{4+} (e.g. [26]). "Region II" behaviour (i.e. subsequent re-softening but still retaining an absolute hardening with respect to the host material) corresponds to the initial formation and subsequent growth of a sub-surface amorphous layer. This layer is softer than the host material. "Region III" (absolute softening) corresponds to doses which are high enough to establish a true *surface* layer of this softer amorphous material.

The variation in low-load (i.e. shallow penetration) hardness of C^+ and N_2^+ implanted glass is shown in Figs. 4 and 5. It can be seen that the behaviour of this material is broadly similar to that of the crystalline sapphire. Again, an initial increase in hardness is observed until peak hardnesses are obtained (at 1.5×10^{16} ions cm^{-2} for both C^+ and N_2^+ implantations). Subsequently, there is a decrease in hardness with further increases in dose until an absolute softening occurs. Similar behaviour has been observed for implantations into soda-lime–silica glass with both N^+ at 25 keV [19] and Ar^+ at 500 keV [20]. Explanations for the

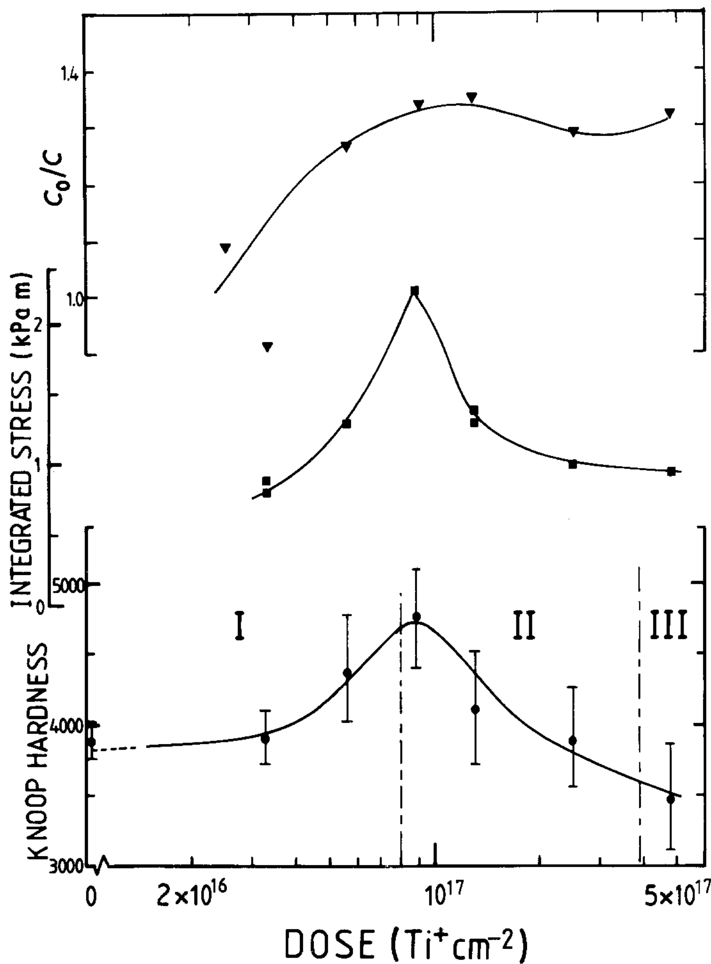

Figure 2 For Ti^+ implanted into sapphire, the curves show the variations with dose of (●) 25 g Knoop microhardness, (■) integrated stress (cantilever bending method), and (▼) radial crack trace length (expressed as the ratio of the unimplanted crack size C_0 to the implanted crack size C) for 200 g Vickers indentations. Note that all three of these parameters peak at similar doses, $\sim 9 \times 10^{16} Ti^+ cm^{-2}$, corresponding to the dose at which amorphization first occurs. The scatter shown in the microhardness results is $\pm\sigma$ (σ is the standard deviation).

hardening phenomena seen in this previous work appear to attribute the rise in hardness to the presence of a compressive stress. However, since the compressive stresses generated by the implantation processes ($\sim$ 165 MPa – see Section 4.3) are considerably less than the yield stress of the glass ($\sim$ 3 to 5 GPa [27]) this explanation appears unsatisfactory. A further factor may be that, besides placing the surface in compression, the injection of large numbers of foreign atoms into the glassy network will fill the spaces within the structure, thus hindering densification – itself known to be important as a deformation mechanism in glasses [27, 28]. However, displacement damage will disrupt the glassy network which perhaps would be expected to lower the flow stress of the surface. Thus, these two effects may be in competition, with the latter effect predominating at higher doses. Additional hardening may arise from the implanted ion species itself forming bonds to the glassy network, as has been suggested by Wang *et al.* [19].

In the case of glass implanted with gaseous ion species at high doses, blisters may be expected to form [29] with a subsequent degradation in mechanical properties. Indeed this is the case for the highest-dose N_2^+ implantation in this study (Fig. 6) where extensive blistering was observed. This coincides with, and probably accounts for, the marked further softening at doses above $\sim 3 \times 10^{17} N_2^+$.

4.2. Surface stress determination: cantilever bending method

The ion-implanted sapphire specimens all showed surface curvatures that were easily detectable using the Talysurf. The deflections

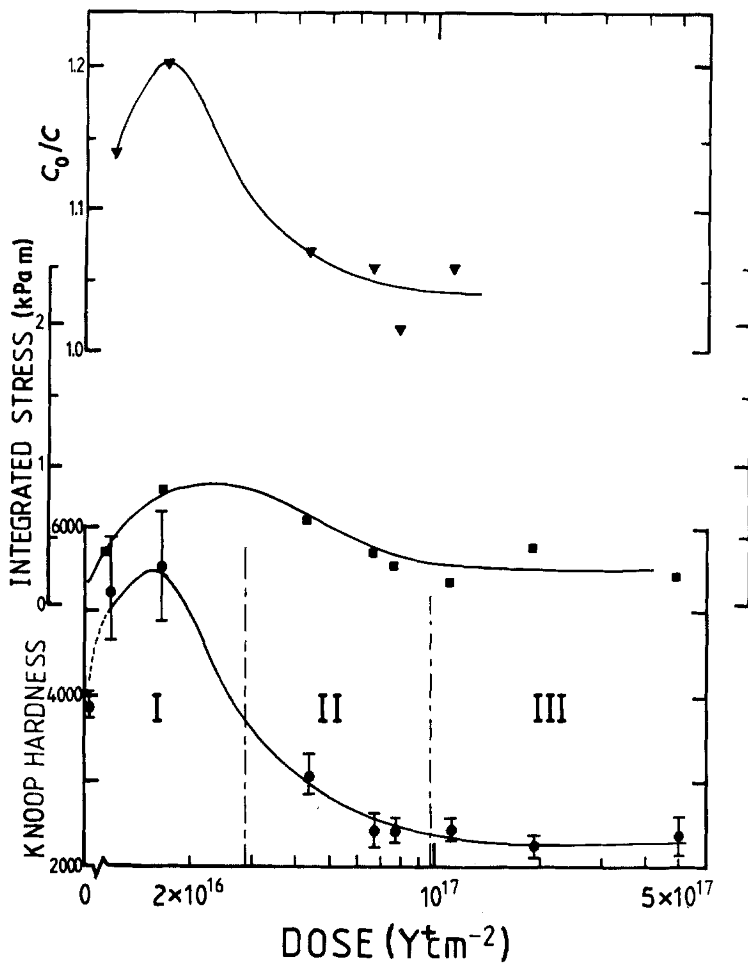

Figure 3 For Y^+ implanted into sapphire, the curves show the variations with dose of (●) 25 g Knoop microhardness, (■) integrated stress (cantilever bending method), and (▼) radial crack trace length (expressed as the ratio of the unimplanted crack size C_0 to the implanted crack size C) for 100 g Vickers indentations. Note that all three of these parameters peak at similar doses, $\sim 2 \times 10^{16}\, Y^+ \,cm^{-2}$, corresponding to the dose at which amorphization first occurs. The scatter shown in the microhardness results is $\pm\sigma$ (σ is the standard deviation).

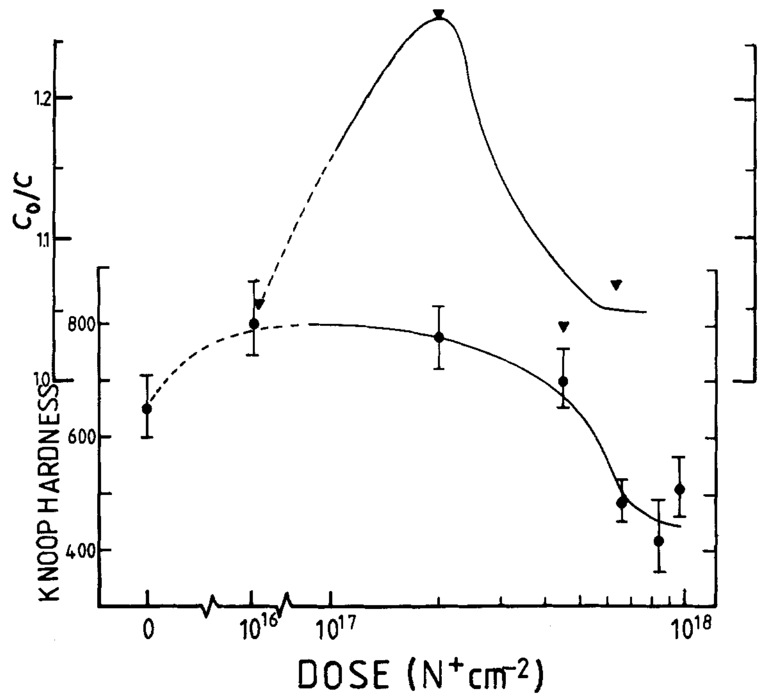

Figure 4 The variations with dose of (●) 10 g Knoop microhardness and (▼) radial crack trace length (expressed as the ratio of the unimplanted crack size C_0 to the implanted crack size C) for 500 g Vickers indentations, for glass implanted with N^+ (note: the dose of N^+ corresponds to 7/4 × dose of N_2^+; see text). Both microhardness and C_0/C reach a peak in the dose range 1 to 3 × 10^{17} $N^+\,cm^{-2}$. The scatter in the microhardness is $\pm\sigma$ (σ is the standard deviation).

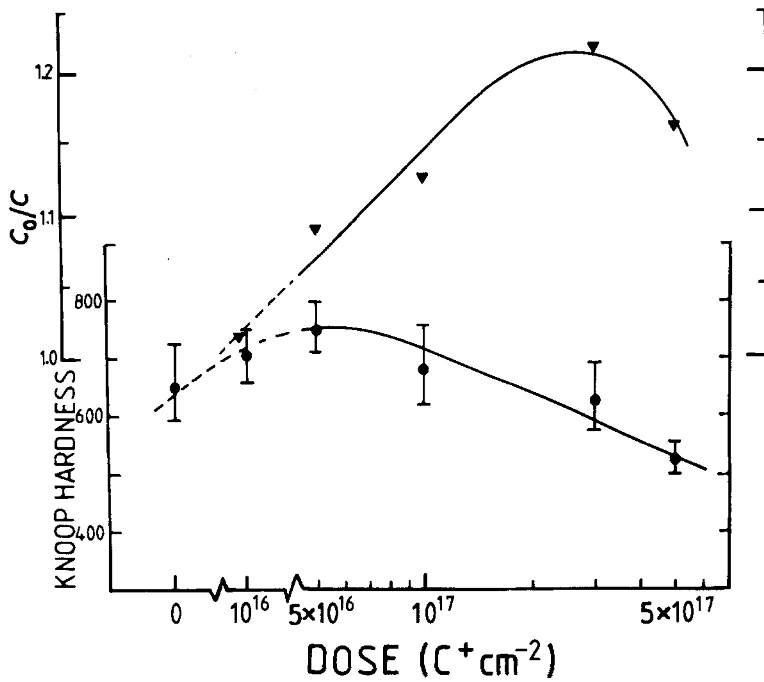

Figure 5 The variations with dose of (●) 10 g Knoop microhardness and (▼) radial crack trace length (expressed as the ratio of the unimplanted crack size C_0 to the implanted crack size C) for 500 g Vickers indentations, for glass implanted with C^+. Both microhardness and C_0/C show peak values at specific doses. However, unlike Figs. 2 to 4, these doses do not coincide with each other.

measured over a 10 to 15 mm track parallel to the long axis of the specimen were in the range ~ 1 to 5 μm. Fig. 7 shows the profiles obtained for the Ti^+ implanted sapphire. Integrated stress values, S (MPa m), were obtained using the method of Eernisse [6, 8] whereby

$$S = \frac{Et^2\delta}{3l^2(1 - \nu)} \tag{1}$$

where E = Young's modulus = 450 GPa, ν = Poisson's ratio = 0.25, t = thickness of cantilever = 0.418 mm, l = length of beam and

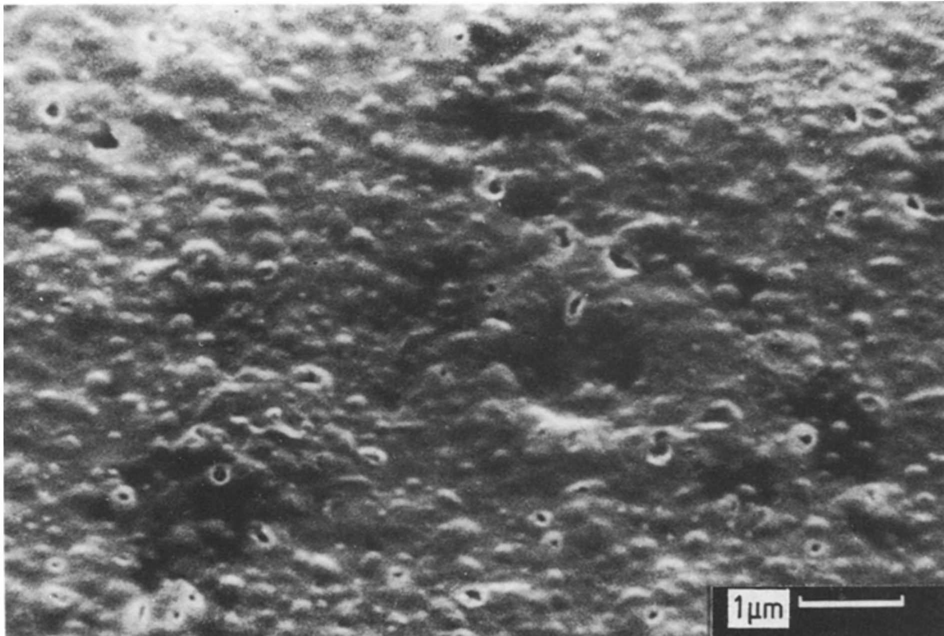

Figure 6 A scanning electron micrograph (secondary electron image, 45° tilt, 30 keV) showing blistering (gas bubble formation) in the surface of soda-lime–silica glass implanted with a high dose of nitrogen ($> 5 \times 10^{17}$ N^+ cm^{-2}).

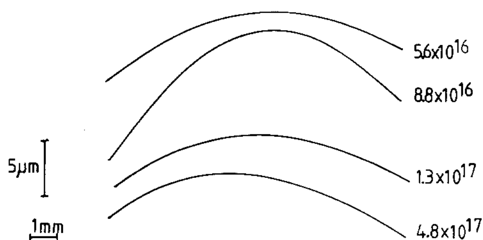

Figure 7 A selection of profilometer traces showing the surface curvature developed on the sapphire cantilever specimens by implantation with Ti^+ to the doses indicated. Note the maximum surface curvature apparent around $8.8 \times 10^{16}\,Ti^+\,cm^{-2}$.

δ = deflection of the beam over the distance l.

For simplicity the sapphire has been assumed to be isotropic with values of E and ν taken from Krefft and Eernisse [6]. Errors due to this assumption are relatively small and of little consequence when purely comparative measurements are being made. S is the stress integrated over the implantation-affected depth and thus represents the total force per unit sample width responsible for the observed bending. Since the implantation-affected zone is always thin ($\lesssim 0.5\,\mu m$) in comparison with the specimen thickness ($418\,\mu m$), S approximates to the force per unit width acting in the surface, and is therefore a useful parameter for comparing the stresses (and hence volume changes etc.) resulting from implantations with different substrates, species and energies, and thus differing depths. Further, if some assumption concerning the stress distribution in the layer is made (e.g. Gaussian; see Section 5), then the maximum stress generated in layers of differing thickness can be computed and compared.

The variations of integrated stresses with dose for Ti^+ and Y^+ implantations into sapphire are shown in Figs. 2 and 3 (and are later re-plotted in Fig. 8). In both cases it may be seen that, at low doses, the integrated stress increases approximately linearly with dose (as previously reported by Krefft and Eernisse [6]) reaching maximum values at "critical doses" of $\sim 9 \times 10^{16}\,Ti^+\,cm^{-2}$ and $\sim 2 \times 10^{16}\,Y^+\,cm^{-2}$. By comparison with the hardness:dose data in Figs. 2 and 3, it is clear that these critical doses correspond to those at which the hardness is also a maximum.

The compressive stresses are principally generated by the volume expansion due to both (a) the production of vacancy/interstitial pairs (i.e. displacement damage by both the primary and knocked-on ions), and (b) the injection of large numbers of foreign atoms into the surface. Since the number of defects produced is expected to be linearly dependent upon dose, it is not surprising that the stresses generated are also linearly dependent upon dose, i.e.

$$S = \alpha\Phi \qquad (2)$$

where Φ = dose and α = constant of proportionality.

Modification to this linear stress dependence may arise from temperature variations (e.g. due to dose rate and poor thermal contact) during the implantation process. In addition, the energy deposited into electronic processes might also be expected to contribute to the total integrated stress. Eernisse, implanting light ions into silica, determined that the contribution of electronic energy deposition processes to stress was sub-linear, dose-dependent and dose-rate dependent [8]. However, the contribution to stress from these processes is expected to be small compared to the displacement damage and will be ignored here.

Beyond the critical dose, stress relief results from the formation of an (initially sub-surface) amorphous layer. The mechanism of stress relief may be attributed to this softer layer expanding vertically in response to the biaxial lateral compressive stresses within it. Clearly, the maximum stress that remains within the amorphous layer can be identified with some sort of "yield stress" for whatever deformation processes occur. An estimate of this yield stress will be made in Section 5. Krefft and Eernisse [6] suggested that matrix slip on $\{0001\}$ may also occur, but, given the strong thermally activated Peierls stress on this slip system [30], this seems unlikely at room temperature. Further, although $\{0001\}$ slip is known to occur around hardness impressions in sapphire at room temperature, material slip during hardness testing is known to be strongly influenced by the large compressive constraints imposed on motion of material displaced by the indenter (e.g. [27]). By contrast, in the present case, the still-crystalline matrix above and below the amorphous layer should be unconstrained and thus slip is less likely.

Figs. 8a and b show plots of integrated stress against both dose and energy deposited as

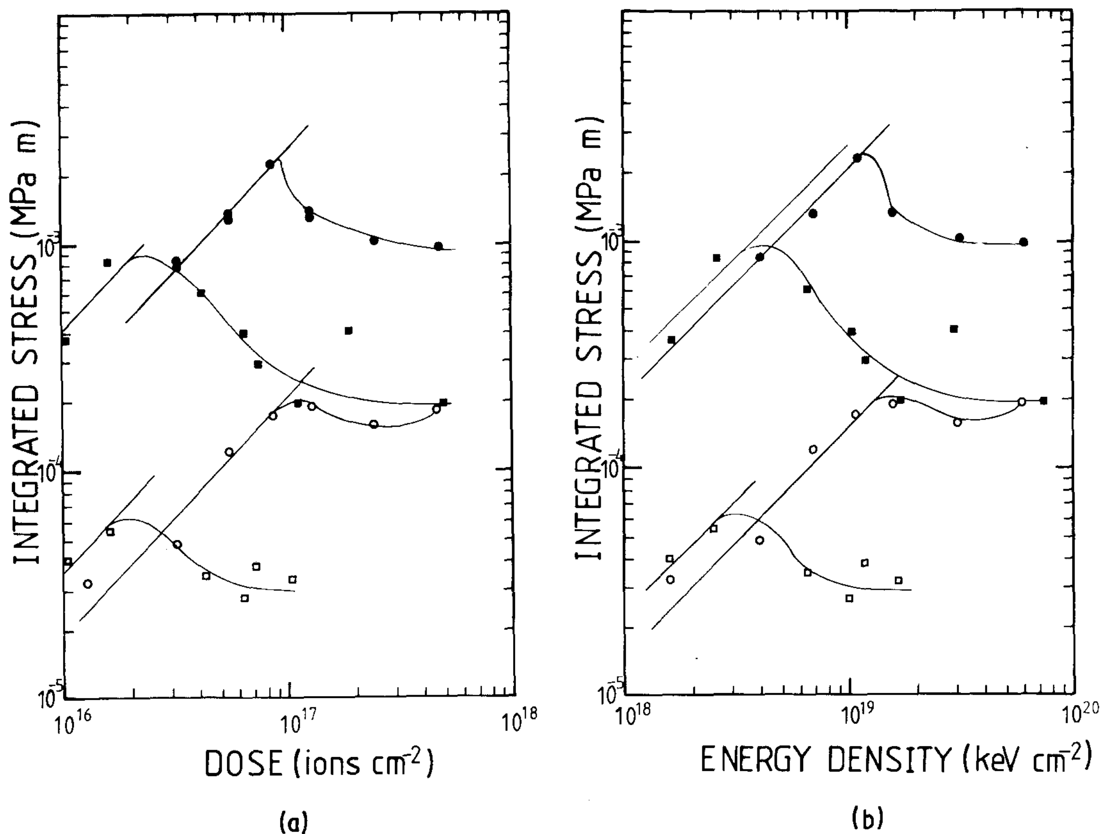

Figure 8 (a) The variations of integrated stress in sapphire with dose of (●, ○) Ti^+ and (■, □) Y^+. The integrated stress values plotted are those determined from both the cantilever bending data (closed symbols) and the indentation fracture (crack length) data (open symbols). It can be seen that both these sets of data show similar forms, a linear increase in integrated stress with dose being found at the lower doses with subsequent relief occurring at higher doses. Note that for both implants, the cantilever bending data yield integrated stresses approximately an order of magnitude higher than the indentation fracture data. (b) As for (a) except that the dose data have been rescaled in terms of displacement damage energy. Note that the linear portions of the two sets of curves are now more nearly coincident.

displacements. Unlike the log–linear plots of Figs. 2 and 3, these log–log plots show the initial linear dependence of S on dose. From Fig. 8a it can be seen that before amorphization occurs, S is less for the Ti^+ implantations than for the Y^+ implantations at equivalent doses. This is expected since S should depend on the level of displacement damage, which is greater per ion for Y^+ (see Table I). In order to take account of this, Fig. 8b shows S re-plotted against total energy deposition per cm^2. The straight-line portions of the Y^+ and Ti^+ curves are now much more nearly coincident.† The remaining discrepancy will be discussed later.

Finally, the surface crazing previously observed in high-dose Y^+ implanted sapphire [10] was also observed to occur here at doses $\gtrsim 10^{17}\,Y^+\,cm^{-2}$. This crazing was previously attributed to the soft amorphous layer being pulled apart as the specimen bent in response to the compressive stresses in the surface. In the present study, it was found that the majority of the crazes were crystallographically oriented perpendicular to the trace of the (0001) plane on the $\{10\bar{1}2\}$ test surface (Fig. 9). This probably reflects the elastic anisotropy of sapphire for which $E \parallel (0001) < E \parallel [0001]$ (425 and 460 GPa respectively), resulting in the maximum

†Note also that the energy densities for amorphization of sapphire by Ti^+ and Y^+ do not coincide in this plot as perhaps might be expected. This is because the energy deposition profile of Y^+ is higher and narrower than that for Ti^+, so local amorphization still occurs at lower total energy depositions.

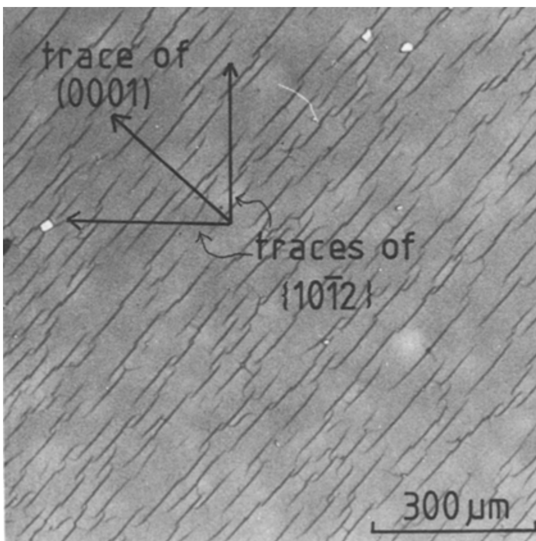

Figure 9 A reflected light micrograph of the crazing observed on the Y^+ implanted sapphire specimens at doses $\gtrsim 10^{17}$ Y^+ cm^{-2}. Note the definite crystallographic orientation of the crazes perpendicular to the traces of (0 0 0 1) (see text for discussion).

elastic strains in the substrate being parallel to the (0 0 0 1) trace. Thus, crazes perpendicular to this strain would be expected. Conversely, it should be noted that crazing due to displacements from (0 0 0 1) slip in the matrix would be expected to be parallel to the (0 0 0 1) traces.

4.3. Surface stress determination: indentation fracture method

As described earlier, ion implantation has been observed to have two main effects on the indentation fracture behaviour of brittle materials. Firstly, a suppression of lateral crack breakouts results (e.g. [11]), together with a suppression of sub-surface lateral crack propagation and/or nucleation (e.g. [10]). These phenomena were observed in the present study for both the sapphire and glass specimens, examples of which are shown in Figs. 10a to d. Secondly, a small but significant decrease in the extent of the radial crack trace on the test surface, yielding apparently increased K_c values by indentation fracture analysis (e.g. [30]), has been observed (e.g. [2–5]). In certain cases, as here, the formation of the median/radial cracks may be suppressed altogether. An example of this is shown in Figs. 11a and b. However, in most cases, only a partial suppression of the median/radial crack system occurs and this has been attributed to compressive stresses creating a back-traction on the crack front in the implantation-affected zone [10]. This is manifested as a change in the crack profile as shown schematically in Fig. 11c. Figs. 11d and e show the actual crack profiles observed in cross-section for unimplanted and implanted glass. The action of the compressive stress is seen to cause a narrowing of the crack trace as it approaches the surface as predicted by Lawn and Fuller [12] and previously shown by us [10]. A tensile stress is expected to produce the opposite effect [12, 13], i.e. a broadening of the crack trace (see Fig. 11c). In this study, careful measurements of the changing crack trace length with implantation has enabled the magnitude of the stress acting in the surface to be deduced using the recent model of Lawn and Fuller [12].

An alternative means by which a measure of the surface stress might be obtained is by determining the variation in frequency of median/radial crack occurrence with dose (e.g. [20]). Examples of this type of data are shown in Fig. 12, which shows the dose-dependence of crack incidence in N_2^+ implanted glass. Less crack suppression was seen in C^+ implanted than in N_2^+ implanted glass. Similarly, above a dose of $5 \times 10^{16}\,cm^{-2}$, Ti^+ implanted sapphire displayed more crack suppression than Y^+ implanted sapphire. However, since there is no well-developed theory to relate the incidence of cracking to dose this approach was not pursued further, but it serves to demonstrate the significant influence implantation can have on cracking. In all cases, changes in crack behaviour (at a given indentation load) are expected to depend on the integrated stress level resulting from particular implantations (see Section 5).

Lawn and Fuller have recently suggested a relationship linking the modification of radial crack length to the level of stress σ_s in a surface layer of thickness d, i.e.

$$1 - (C_0/C)^{3/2} = \frac{2\psi\sigma_s d^{1/2}}{K_c} \quad (3a)$$

$$= \frac{2\psi S}{K_c d^{1/2}} \quad (3b)$$

where K_c = substrate toughness, C_0 = radial crack length at zero stress, C = modified crack length at stress = σ_s and ψ = constant ($\simeq 1$)

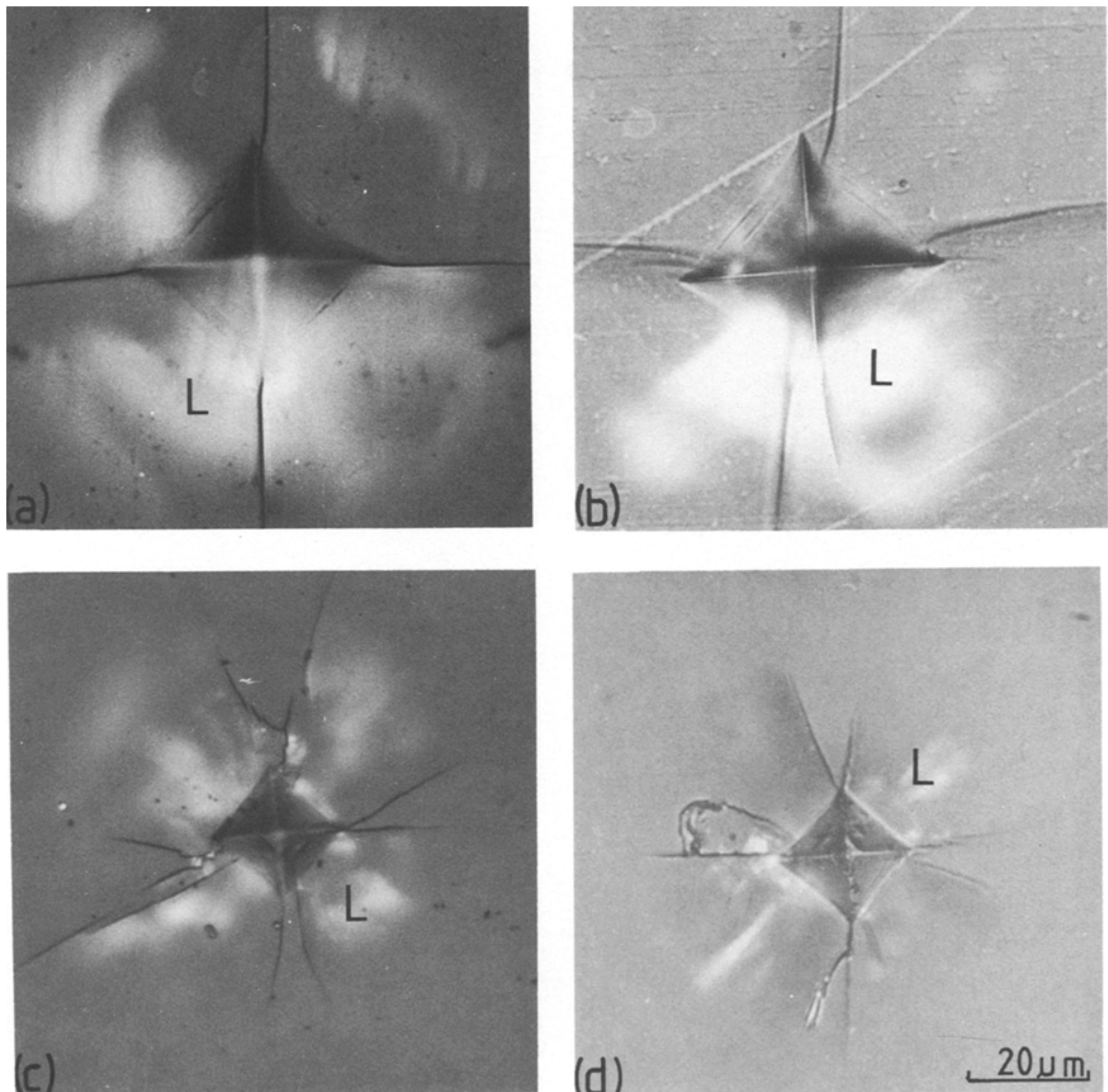

Figure 10 Reflected light micrographs of 500 g Vickers indentations made in (a) unimplanted soda-lime-silica glass; (b) 2.6×10^{17} N_2^+ cm^{-2} implanted soda-lime-silica glass; (c) unimplanted sapphire; (d) 6×10^{16} Ti^+ cm^{-2} implanted sapphire. Note that around the indentations in the unimplanted material there is extensive contrast (L) arising from sub-surface lateral cracking. The implanted specimens show reduced sub-surface lateral cracking.

dependent upon crack geometry; hence for $C < C_0$, σ_s is the negative i.e. the stress is compressive. Thus, the integrated stress $(\sigma_s d)$ should be a function of C_0/C i.e. when C_0/C is a maximum, S should also be a maximum. For sapphire, C_0/C has been plotted against dose along with the hardness and S values in Figs. 2 and 3. For both Ti^+ and Y^+ implanted sapphire, there is a good correlation between the peak hardness, peak stress and peak value of C_0/C, all of which correspond to the approximate dose at which amorphization occurs.

For glass, C_0/C has also been plotted against dose (Figs. 4 and 5) but the correlation between peak hardness and peak C_0/C values is less clear. As previously discussed, the mechanisms that give rise to hardening and/or compressive stresses are less well understood in glasses, and thus behaviour similar to that of crystalline materials need not necessarily be expected. For both Ni^+ and C^+ implantations, peak C_0/C occurs at higher doses than the peak hardness and we have no explanation for this phenomenon.

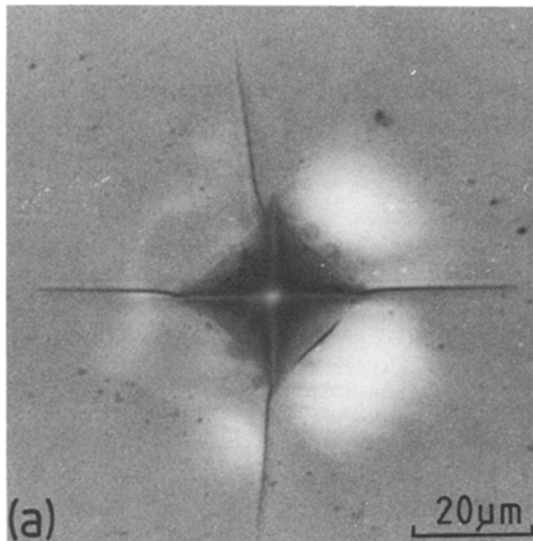

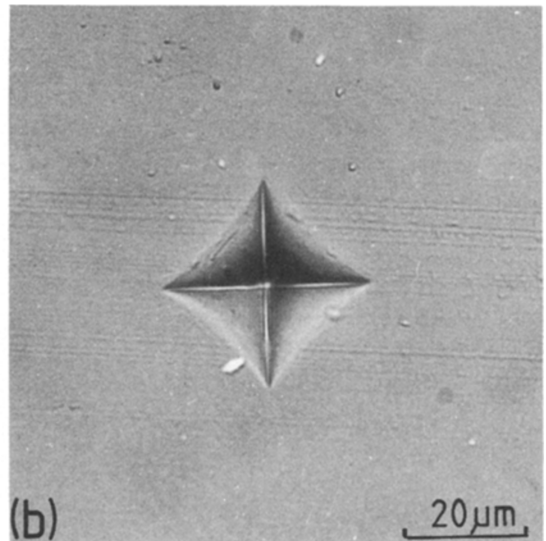

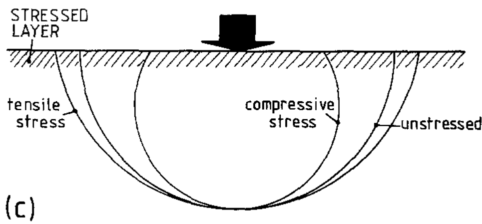

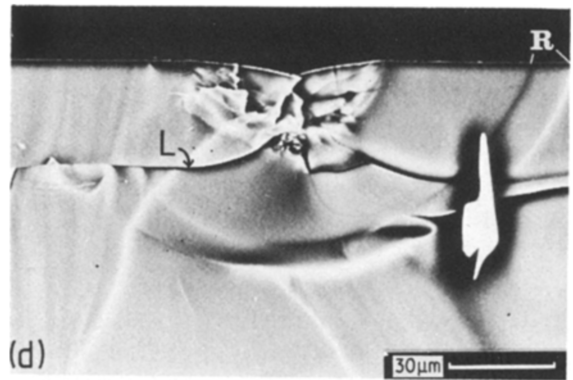

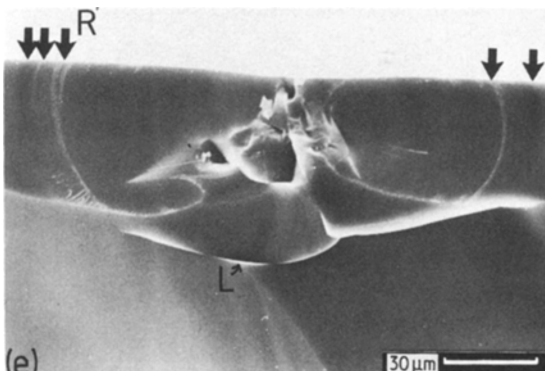

Figure 11 (a) Reflected light micrograph of a 300 g Vickers indentation in unimplanted glass. (b) As (a), only in glass implanted to $1.1 \times 10^{17}\ N_2^+\ cm^{-2}$. Note the total absence of any indentation fracture in (b). (c) Schematic representation of the expected modifications to the radial/median crack profiles resulting from the presence of either compressive or tensile compressive stresses. (d) Cross-section of a 300 g Vickers indentation in unimplanted glass, showing both the semicircular traces of successive positions of the radial/median crack (R) and the presence of sub-surface lateral cracks (L). (e) Cross-section of 300 g Vickers indentation in $3 \times 10^{17}\ C^+\ cm^{-2}$ implanted glass, showing the oblate radial/median crack profile (R′) expected in the presence of a surface compressive stress together with modified lateral crack morphology.

In terms of indentation fracture mechanics, the consequence of shortened radial crack traces upon fracture toughness values is obvious. Using the equation due to Lawn and co-workers [31, 32] for radial cracking around a Vickers indentation the fracture toughness K_c may be found from

$$K_c = 0.0139\ (E/H)^{1/2} P C^{-3/2} \tag{4}$$

where H = hardness, E = elastic modulus and P = load. Fig. 13 shows this variation of apparent K_c with dose (at selected loads) for all

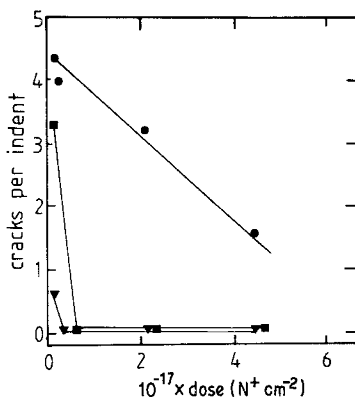

Figure 12 The variation of radial crack frequency with dose for N^+ implantations into glass: load (▲) 100 g, (■) 200 g, (●) 500 g. Note the complete radial crack suppression that occurs after implantation at the lower loads (100 and 200 g).

the ion/substrate combinations used in this study. Since hardness is a function of indentation size (and thus load) (e.g. [33, 34]) the values of H used in Equation 3 were selected as those appropriate to the values of the loads P. It can be seen that apparent increases in K_c of up to 50% are observed. It is also clear from Fig. 13 that there are limited dose ranges over which maximum surface toughness increases may be obtained.

Using the values of K_c (from Equation 4) determined for the unimplanted control specimen, knowing C and C_0 and assuming an implanted layer thickness of $4\langle \Delta X_D \rangle^\ddagger$, Equation 3 can be used to calculate σ_s and hence S. For sapphire, this integrated stress S is plotted against both dose and energy deposition in Fig. 8, together with the S values obtained by the cantilever bending studies described in Section 3.3. An obvious feature of this figure is that the apparent integrated stresses calculated from the changing crack length behaviour are consistently lower than those values obtained from the cantilever studies by approximately the same amount (i.e. $\times$ 10 for both Ti^+ and Y^+ implantations).

For glass, it can be seen that the integrated stresses for both N^+ and C^+ peak at approximately the same dose as shown in Fig. 14. When re-plotted in terms of energy deposition (as performed for sapphire in Fig. 8b, it is found that the two curves become more widely separated, whereas they might be expected to merge. This suggests that errors in dose measurements etc. may be manifest here. However, it is interesting to note that the slopes of the S–dose lines for glass are ~ 0.5 rather than the expected value of 1.0. Thus, an alternative explanation for the forms of the graphs in Fig. 14 could be that all the data have been taken at doses above the linear portion of the dose–stress relationship, i.e. linear behaviour with full merging of the S–energy-density curves would have occurred at lower doses as reported by Eernisse [8].

5. Surface stress modelling

To our knowledge, no attempt has yet been made to describe quantitatively the stress relief observed at high-dose implantation. The previous sections of this paper have clearly established the link between the onset of amorphization (as monitored by hardness response) and the onset of stress relief. Consequently, we have devised a simple model which describes the role of amorphization in stress relief and this will now be described.

As described in Section 2, the surface stress originates from the volume expansion caused by the creation of defects (by displacement damage) together with the injection of a large number of foreign atoms into thin layers. Both the damage and range distribution may be assumed Gaussian in form and the total integrated stress may be obtained by summing the local stress contributions from these profiles. Prior to amorphization both the implant concentration and the damage vary linearly with dose (assuming a constant annealing rate, if any, and no sputtering) and thus the integrated stress is expected to rise linearly with dose (see Section 4.1). However, after amorphization the integrated stress may be considered to be the sum of those contributions from the portions of the damage and range profiles lying in the still-crystalline material, together with that from the stress supported within the amorphous layers. Since, from the hardness results, we know that the amorphous layer is softer than the host material, it is expected that the maximum stress supported in the amorphous material will be less than the

$^\ddagger \langle \Delta X_D \rangle$ is the standard deviation in the depth of the damage peak position, i.e. if the distribution is asumed Gaussian then 96% of all damage will lie in a layer $4\langle \Delta X_D \rangle$ thick.

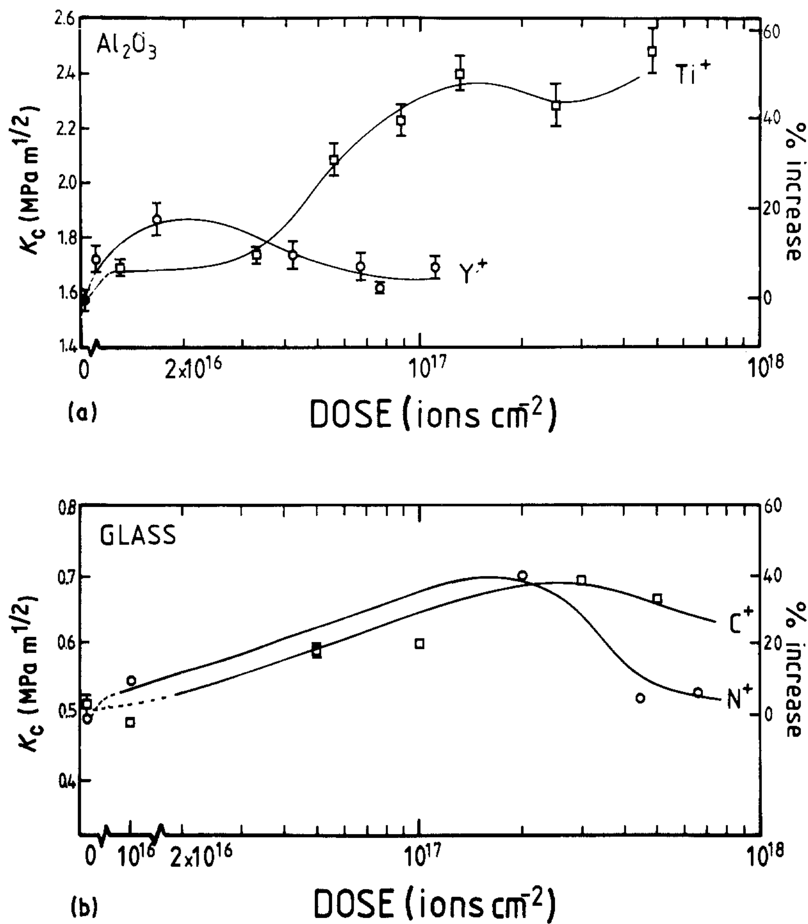

Figure 13 (a) The variation of indentation fracture toughness (K_c) with dose for Ti^+ and Y^+ implantations into sapphire. Apparent increases in fracture toughness of up to ~50% may be obtained in some cases. (b) As (a) but for implantations of C^+ and N^+ into glass. In this case improvements in K_c of up to ~40% are obtainable. The data in both of these figures are obtained from combining the results of tests made at several different loads. The indicated scatter in the data is $\pm\sigma$ error in the mean. Essentially, these curves reflect the change in C_0/C shown in Figs. 2 to 5.

maximum stress in the crystalline material on either side of it. Hence stress relief is expected. Thus, the model is based on the following assumptions:

(i) the variation of S with dose (and hence energy deposition) is assumed to be linear prior to amorphization. Thermal effects, dose rate, electronic effects etc. have been neglected;

(ii) the thickness of the amorphous layer and its spatial position (i.e. surface or sub-surface) has been evaluated using our previous model [1] and the amorphous material is assumed to be mechanically homogeneous;

(iii) after amorphization the compressive stress in the surface is taken to consist of two components, the stress supported within the still-crystalline but damaged material (S_c) and a component of stress supported within the now amorphous material (S_a). The former stress component will arise from two sources, namely the volume expansion directly due to the presence of the implanted atoms (S_{ca}) and the volume expansion due to the formation of other defects, e.g. Frenkel pairs (S_{cd}). The levels of stress attributed to these two components will be directly proportional to the fraction of their Gaussian profiles lying outside the amorphous layer. The separation of S_{ca} and S_{cd} is necessary since the concentration and damage profiles are not coincident, e.g. while amorphization begins at the peak of the damage profile, the peak of the concentration profile is always deeper than this and may still lie in crystalline material.

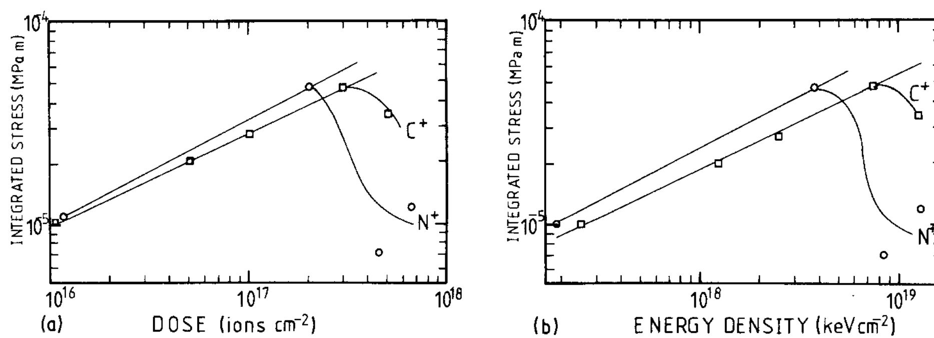

Figure 14 (a) The variation of integrated stress with dose for glass implanted with both C^+ and N^+. The integrated stress values are evaluated from the crack length data of Figs. 4 and 5 using Equation 3 (see text). (b) As (a), only the dose data have been rescaled in terms of energy available for displacement damage.

Fig. 15 illustrates schematically the operation of the model for the three microstructural regimes described in Section 2 (and Fig. 1) with arbitrary low stress being supported in the amorphous material. For clarity S_c has not been split into its two components S_{ca} and S_{cd}.

Thus, once the range and damage profile have been obtained, the model is controlled by four parameters, namely:

(i) the constant of proportionality α from Equation 1 (Section 4.2) which may be determined experimentally;

(ii) the stress supported within the amorphous layer, σ_a;

(iii) the partitioning of the stress contributions from the still-crystalline materials into components due to the damage (S_{cd}) and due to the implanted atoms (S_{ca}), which may be represented as $\beta = S_{ca}/(S_{cd} + S_{ca})$; and

(iv) the critical energy density at which amorphization occurs ($\varrho_{E_{crit}}$), which may also be determined experimentally (e.g. [10]).

Fig. 16 illustrates the dose against integrated stress behaviour predicted for the case of β being small (i.e. the stress in the crystalline material is damage controlled), and the amorphous layer supporting stresses in the range zero to σ_{max} where σ_{max} is the stress in the crystalline at the onset of amorphization (i.e. the maximum stress level obtainable). The salient features of these results are:

(i) if the amorphous layer supports no stress, then the integrated stress falls off dramatically after amorphization due to the initial rapid thickening of the amorphous layer, though at higher doses the stress maintains a nearly constant value;

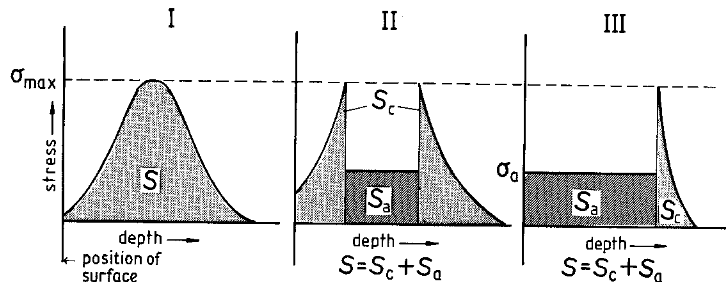

Figure 15 A schematic representation of the principles of the implantation-induced stress model. Initially, at doses below that for amorphization (Region I), the integrated stress S is the sum over the implanted depth of the expected stress profile arising from implantation. Upon amorphization (Region II) the integrated stress is the sum of the portion of the Gaussian implant profile remaining within the crystalline material, S_c, and the stress level supported within the now amorphous material, S_a. σ_a (the stress-supporting capability of the amorphous material) is assumed to be less than σ_{max}, the stress supported within the crystalline material at the point of amorphization. At higher doses a surface amorphous layer is formed (Region III) and the stress contribution from the crystalline material is further reduced.

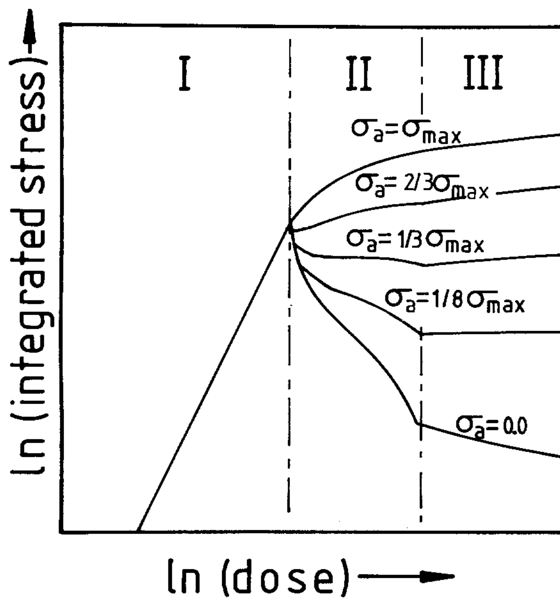

Figure 16 A schematic representation of the integrated stress levels predicted by the model over the three microstructural regimes I, II and III, for amorphous layer stresses in the range σ_{max} to zero. For $\sigma_a \gtrsim \frac{1}{2}\sigma_{max}$, the integrated stress continues to rise after amorphization with increasing dose. For $\sigma_a \lesssim \frac{1}{2}\sigma_{max}$, stress relief occurs upon amorphization and a sharp drop in integrated stress is predicted (see text).

(ii) if $\sigma_a = \sigma_{max}$ the integrated stress will continue to rise after amorphization, again gradually levelling off at higher doses, and
(iii) intermediate values of σ_a (e.g. $\frac{1}{8}$ to $\frac{1}{3}\sigma_{max}$), an initial decrease in integrated stress will be observed; however, by the time Region III is reached, S may start to increase slowly.

Applying this model to the cantilever-bending integrated stress results obtained for Ti^+ and Y^+ in sapphire shows clearly that the parameters in the model are capable of being fitted to the experimental data (Fig. 17), best-fit values being given in Table II. For example, for Ti^+ implants into sapphire the data can be seen to fit well to the behaviour predicted for $\sigma_a = 2$ GPa. Interestingly, this figure, if assumed to be the yield stress of the amorphous material, correlates well with the estimated Vickers hardness of the soft amorphous layer, i.e. taking $H \simeq 3Y$ (for a fully ductile solid) gives a Vickers hardness of ~600 VHN, a previous estimate§ being 500 to 1500 VHN [10]. For Y^+ implanted sapphire, the data can be seen to fit well to the dose against integrated stress behaviour predicted for $\sigma_a = 0$. Initially this may seem to contradict the prediction made for the Ti^+ implanted layer. However, in Section 3.2 (Fig. 8), we saw that the amorphous surface of the Y^+ implanted specimen crazed at doses of $\gtrsim 10^{17}\ Y^+\ cm^{-2}$ and thus this layer is no longer supporting any stresses, i.e. $\sigma_a = 0$.

Best-fit values of β were found to be small (<0.2; i.e. $S_{cd} \gg S_{ca}$) and this is reasonable since each in-going produces a large number of defects. In order to provide an alternative estimate of β, it was assumed that all implanted ions come to rest in interstitial sites (either tetrahedral or octahedral in α-Al_2O_3) and give rise to a calculable volume expansion. Then, for a given ion dose, the contribution to the total integrated stress by the implanted atoms may be assessed by comparing the expected volume expansions with the observed bulk expansion given variously by Eernisse [6, 8] as

$$\frac{\Delta V}{V} = 3\sigma_s \frac{(1-\nu)}{E} \quad (5)$$

or by King *et al.* [9], in terms of surface displacement, as

$$\frac{\Delta V}{V} = \frac{U_s}{d} = 2\sigma_s \frac{(1-\nu^2)}{E} \quad (6)$$

TABLE II Stress-model parameters used to fit the experimental data for sapphire

Ion species and energy	Experimentally determined		Best-fit variables	
	Constant of proportionality α (MPa m per ion)	Critical energy density for amorphization $\varrho_{E_{crit}}$ (keV cm^{-3})	Stress partitioning coefficient β	Stress supported by the amorphous layer σ_a (GPa)
Ti^+ 300 keV	2.6×10^{-20}	8.0×10^{23}	0.17	2.0
Y^+ 300 keV	4.5×10^{-20}	6.0×10^{23}	0.05	0.0

§ Since in our dose ranges we have no specimen available with a surface amorphous layer due to Ti^+ implantation, this estimate is for the amorphous layer on sapphire implanted with $>10^{17}\ Y^+\ cm^{-2}$.

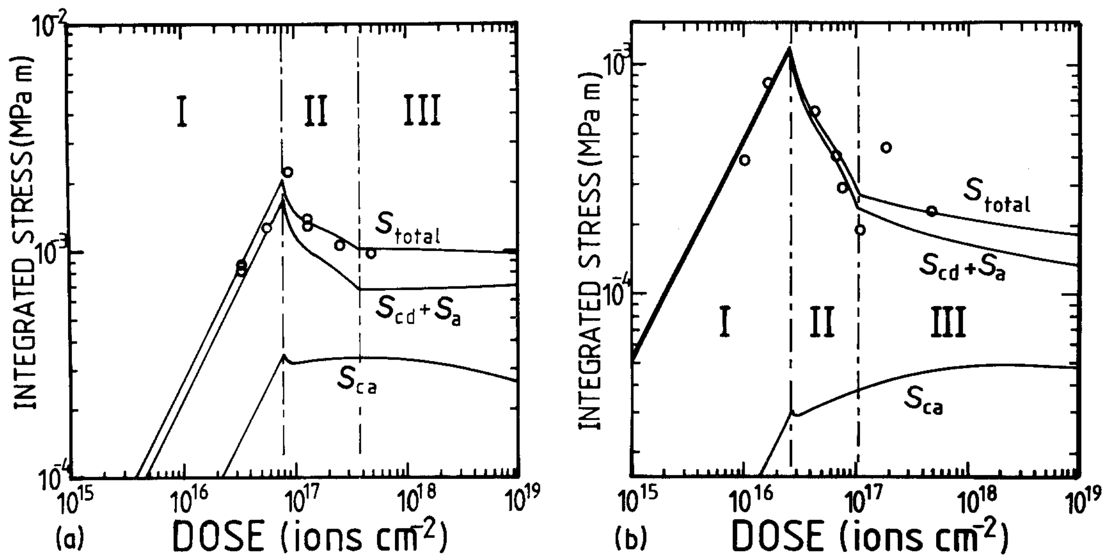

Figure 17 (a) The integrated stress model fitted to the experimentally-obtained integrated stress data for Ti^+ implanted sapphire ($\beta = 0.17$, $\sigma_a = 2000$ MPa) (see Table II for full details). (b) The integrated stress model fitted to the experimentally-obtained integrated stress data for Y^+ implanted sapphire ($\beta = 0.05$, $\sigma_a = 0$). In both (a) and (b) the predicted integrated stress has been apportioned (using β) into contributions from the volume expansion due directly to the implanted ions, S_{ca}, and that due to the sum of the implantation-induced damage and the stress supported in the amorphous layer, ($S_{cd} + S_a$). Note that S_{ca} continues to rise after amorphization into Regions II and III, due to the implant profile peak lying deeper than the displacement damage profile peak.

where σ_s = mean lateral stress and U_s = vertical expansion.

Assuming homogeneous expansion of the coordination polyhedra around each site type, the changes in volume due to both host and implanted ion species occupying interstitial sites were evaluated. These volume expansions are given in Table III. Taking the data for representative specimens implanted to doses beneath those for amorphization, the changes in volume of the implanted layer were estimated from the mean stress σ_s, assuming that S extends over a layer $4\langle \Delta X_D \rangle$ thick (see Table IV). Using Equation 5, $\Delta V/V$ was calculated and thus ΔV estimated for the layer $4\langle \Delta X_D \rangle$ thick. In order to calculate the proportion of this volume occupied by the implanted species, some assumptions had to be made concerning both the charge state and location of ions In both cases, the site giving the largest volume expansion was chosen from Table III in order that an upper-bound estimate of the volume increases due to the implant profile could be made (i.e. Ti^{3+} in octahedral interstices and Y^{3+} in octahedral interstices). From Table IV it can be seen that the maximum volume strains expected from

TABLE III Calculated volume expansions for implanted ions occupying interstitial sites in sapphire

	Ion species			
	Al^{3+}	Ti^{3+}	Ti^{4+}	Y^{3+}
Ionic radius (nm)*	0.051	0.076	0.063	0.089
Volume expansion for tetrahedral interstice† (nm^3))	9.8×10^{-4}	2.46×10^{-3}	1.64×10^{-3}	3.38×10^{-3}
Volume expansion for octahedral interstice† (nm^3)	0	3.32×10^{-3}	1.20×10^{-3}	5.72×10^{-3}

*From [35].
† Based on close-packed oxygen ions with an ionic radius of 0.132 nm.

TABLE IV Experimentally determined stress levels and volume expansions for implanted sapphire

Implant	Measured integrated stress S (MPa m)*	Stress averaged over $4 \times \langle X_D \rangle = \sigma_s$ (GPa)	Observed ΔV from Equation 5 (nm^3)	Estimated ΔV due to implant (nm^3)†	% volume due to implant
5.6×10^{16} Ti^+ cm^{-2}	1.28×10^{-3}	6.4	7.2×10^{14}	$\sim 1.8 \times 10^{14}$	26
1.7×10^{16} Y^+ cm^{-2}	8.57×10^{-4}	7.6	4.7×10^{14}	$\sim 9.7 \times 10^{13}$	20

*Taking $E = 450$ GPa and $\nu = 0.25$.
†Based on the largest expansion in Table III.

the implant species occupying the smallest interstitial sites are $\sim 26\%$ for Ti^+ and $\sim 20\%$ for Y^+. As expected, the corresponding values of β (0.26 and 0.20) are larger than those estimated from the best fit to the experimental data, but then it is unlikely that all the implanted species occupy the smallest sites. Also radiation damage (annealing) would be expected to relax the structure into less strained configurations.

6. Discussion

The preceding sections have described the techniques employed in this study together with the results obtained. There are, however, a number of points concerning both the accuracy of the data and the interpretation of the results that require further discussion. For convenience these points will be grouped under separate heatings for experimental procedures and results.

6.1. Discussion of experimental procedures

In some cases, it was noticed that the implantation-induced colour and reflection changes were not uniform along the length of the specimen, localized changes occurring near the point of attachment. These observations indicate that either the implantations were not uniform (possibly due to charging of the specimen deflecting the ion beam) or that non-uniform annealing occurred as a result of temperature variations across the specimen.

The former effect appears unlikely to be significant, since studies have shown that the surface of sapphire becomes electrically conducting at doses of $\sim 10^{16}$ ions cm^{-2}. In addition, the glass-slide sections and metal discs upon which the specimens were mounted appeared uniformly discoloured around the specimen, indicating uniform implantations.

The second explanation appears much more likely. Since the specimens were only attached to their mounts at one end, it is probably that there would be a thermal gradient along the length of the specimens. Thus, the unattached end of the specimen would be expected to be less damaged and/or have a thinner amorphous layer present. However, these errors are thought to be small since the 10 mm of specimen length (total 20 mm) farthest away from the attachment point were used for profilometry and indentation tests.

The limitation in accuracy and reproducibility of the Talysurf apparatus means that the surface deflections can probably be measured to $\pm 0.05\,\mu$m. The implanted sapphire was assumed to be perfectly flat, but in fact this may not have been the case. The manufacturer's specification quotes a maximum "bow" of $\sim 3\,\mu$m across the diameter of the uncut 3 inch (75 mm) wafers. In fact, a *concave* bow of 0.3 to 0.4 μm was measured along a 10 mm track on a large unimplanted control specimen. Thus, this error is small compared to the larger deflections measured here but may be significant for the smaller ($\sim 1\,\mu$m) deflections. Since the bow introduced by the wafer manufacturing processes is of the opposite sense to that induced by implantation, then an underestimate in the surface compressive stresses will result at low doses. Thus, the value of S calculated are at worst in error by $\sim 50\%$ and at best by $\sim 5\%$.

Finally, the assumption of elastic isotropy may introduce further errors in the value of S but these are not likely to be more than $\pm 10\%$, and for comparative measurements these are of no consequence.

When calculating the amorphous layer thickness (used subsequently in the stress model) using the model of Burnett and Page [1], a simple, symmetrical Gaussian damage profile was employed rather than the skewed profile evaluated by the EDEP–1 computer code. Neither profile type is believed to be a true representation of the damage profile, the Gaussian being rather simplistic whilst the EDEP–1 profile is known to overestimate the damage

created at the surface [22]. The difference between the amorphous layer thickness calculated using both profiles is small and of no consequence when considered with respect to the inherent limitation of both models.

6.2. Discussion of results

If the critical energy density for amorphization is calculated for both the Ti^+ and Y^+ implants using the approach detailed by Burnett and Page [10], then there are both differences between the values obtained for Ti^+ and Y^+ implants here and between these values and that calculated by them [10]. The former discrepancy may be accounted for by differences in the implantation conditions. The amorphization behaviour of sapphire is known to be temperature-sensitive, and hence variations in temperature as a result of dose-rate/current density differences may well affect the critical energy for amorphization. This is undoubtedly also the root of the discrepancy between the integrated-stress–energy-density plot for the implanted sapphire shown in Fig. 8. Here the integrated stress was normalized against the energy available for displacement damage, and in an ideal case, the stress data prior to amorphization from both the Ti^+ and Y^+ implantations should have laid on a single "universal curve". An additional contribution to the discrepancy may be errors in the energy partitioning calculated using the EDEP-1 code (see Matthews [22] for a discussion). In fact, our previous estimate of $\varrho_{E_{crit}}$ ($\sim 3 \times 10^{23}$ keV cm^{-3} or ~ 44 kJ mm^{-3}) was calculated using the model of Winterbon *et al.* [17], and this probably accounts for the discrepancy between this earlier value and the current values of 6 to 8×10^{23} keV cm^{-3} (~ 88 to 120 kJ mm^{-3}).

The use of indentation techniques for the monitoring of the change in hardness of surface layers has been extensively discussed by us elsewhere [1, 10]. However, the low-load Knoop microhardness results obtained here are thought to be at least a qualitative measure of the changes occurring.

The use of the indentation fracture technique inherently results in a large degree of scatter in both the crack-lengths measured and the subsequently calculated values of K_c and S. However, repetition of the experiments presented here have yielded identical trends even if the calculated values of K_c differed somewhat.

The relation used to derive K_c is not thought to give accurate absolute values [31]; however, for the comparative tests undertaken here it was not necessary to use the later forms of this equation (e.g. that detailed by Anstis *et al.* [32].

Despite the inherent scatter of crack sizes, the crack oblation observed in Fig. 11e seems a genuine effect, it being rather more pronounced in the glass specimens than in the sapphire specimens. This probably stems from the glass possessing neither elastic anisotropy nor preferred crystallographic cleavage planes.

The model proposed by Lawn and Fuller [12] relating crack-shortening to stresses in the surface provides a simple way of determining the surface stress state. However, as a consequence of the crack-length scatter encountered in most brittle materials, this technique is inherently less sensitive than cantilever bending. Lawn and Fuller obtained reasonable correlation between the crack extension data (of Jensen *et al.* [13]) in proton-irradiated silica (irradiated to a depth of 5 μm) and the cantilever bending results of Eernisse. However, in the present study the model was found to yield integrated stresses 6 to 10 times less than those obtained from the beam-bending data of the same specimens. Also, the thickness ($\sim 0.2\,\mu$m) of the implanted and stressed layer is much less than the indentation depth, and in such cases Lawn and Fuller themselves predict an underestimation of the surface stress.

An attempt at modelling empirically the stress-relief associated with amorphization has resulted in a simple model that provides good correlation with the stress data obtained. The accuracy of this model is limited by the assumption of a sharp crystalline to amorphous transition, with an associated abrupt change in mechanical properties. With a more detailed knowledge of the transition in mechanical properties between the crystalline and amorphous materials the model could be refined, thus smoothing the sharp discontinuity in stress predicted to occur upon amorphization as seen in Figs. 16 and 17. Further, whilst it is valid to assume isotropic behaviour of the amorphous material, the elastic anisotropy of the crystalline material should not be ignored in a more detailed model.

Having stated the reservations above, our simple model with two experimentally deter-

mined and two adjustable parameters (i.e. α, the rate of increase of S with dose; $\varrho_{E_{crit}}$, the amorphization criterion; the relative contributions to the stress from the damage and concentration profiles; and σ_a, the stress supported in the amorphous layer) provides good agreement with experimental observations. Thus, for the Y^+ implant it is known that crazing of the amorphous material occurs in response to the cantilever bending of the specimen and, in this case, a good fit is found with $\sigma_a = 0$. However, for the Ti^+ implant a good fit is found with $\sigma_a = 2$ GPa, which is a stress value closely related to the hardness value of amorphized alumina layers estimated from earlier independent experiments [10].

Our calculations of the strains likely to arise from the implanted species being introduced into the structure are probably best viewed as fairly crude estimates. Not only is there uncertainty as to which structure sites or range of sites the implanted ions might occupy, but the final charge state (and thus effective size) of the implanted ions are unknown (though some EXAFS studies of this topic have been made [36]). Further, our calculations are based on site occupancy in an undistorted crystal. Since implantation renders the substrate increasingly damaged, not only will our calculations overestimate the strain contributions in the crystal but these strains will probably vary with position in the damage profile. However, at worst the calculations suggest that a small but substantial part of the strain ($< 20\%$) occurring arises from the implanted ions themselves.

Since displacement damage events outnumber the implant species by $\sim 1000:1$, the fact that the implant profile contributes to the strain at all suggests that substantial levels of both self- and radiation-annealing must be occurring.

Implantation of C^+ and N^+ into soda-lime–silica glass produced hardness and integrated stress behaviour broadly similar to that observed for the Ti^+ and Y^+ implants into sapphire. The integrated stresses were observed to increase with increasing dose (though not linearly) and to reach maximum values before stress relief occurred. However, unlike our sapphire results, we have no microstructural mechanisms to account for the hardening and stress-relief behaviour, though the compressive stress almost certainly arises from a mixture of ion-stuffing and defect production. At high doses of N^+ ($\sim 8 \times 10^{17}$ ions cm^{-2}), blistering of the glass surface was observed to occur and is presumed due to extensive gas-bubble formation. Concomitant softening of the samples was observed, and this behaviour is similar to that reported for other high-dose gaseous ion implantations into both crystalline and non-crystalline materials [29].

Integrated stress values for the glass showed maximum values of $\sim 5 \times 10^{-4}$ MPa m in the implantation-affected layer. However, these values were obtained using the indentation fracture method and, in the light of the sapphire results, the glass data may well underestimate the true integrated stresses. Since the scales of the damage and indentation are similar for both glass and sapphire, and since the underestimates of the Lawn and Fuller model is believed to result from the very narrow extent of the stressed layer, it might be expected that the underestimate would be similar to that observed for sapphire (i.e. $\sim \times 10$).

7. Conclusions

Ion implantation of energetic Ti^+ and Y^+ ions into sapphire has been shown to create compressive stresses in the near-surface (implantation-affected) region of single-crystal sapphire samples. The stress has been observed and measured both by the cantilever bending of thin specimens and by the reduction in extent of radial cracks around Vickers hardness indentations. The only currently available model for indentation fracture behaviour in the presence of a thin highly-stressed layer seems to produce an underestimate of the stress by a factor of ~ 10 when compared to the cantilever experiments. The stress also causes crazing of the amorphous surface layer produced in high-dose Y^+ implanted sapphire.

Since the stress is expected to vary over the damage/implantation profile, integrated stress values of S, as calculated by Eernisse's cantilever bending approach, provide a quantitative means of comparing the stresses produced by different implant/energy/range/damage patterns. Typical maximum integrated stress values were found to be 10^{-3} MPa m with estimated values of the maximum stress being 1 to 10 GPa.

The integrated stress was found to be proportional to dose (i.e. damage/implantation

concentration) for both implants into sapphire. However, in both cases stress relief was observed, which by comparison with a previous model and experiments corresponds to the development of amorphous material near (and finally at) the specimen surface. Thus the production of amorphous material results in stress relief, suggesting that the amorphous material has a lower load-bearing capability in both cases. Transposition of the S–dose plots into S–energy-deposition plots (i.e. correcting for different ion-damage characteristics) produces nearly identical behaviour for the two implants, the residual difference probably resulting from differing implantation conditions (e.g. dose rate and temperature). Further, calculation of the critical energy density required for amorphization yields nearly equal values for the two implantation species of $\sim 7 \times 10^{23}\,\mathrm{keV\,cm^{-3}}$ ($102\,\mathrm{kJ\,mm^{-3}}$).

Estimates of the strains produced by the implant species residing in different sites in undamaged alumina suggest that up to some 20% of the stress is produced by the "ion-stuffing" effects of the implant profile, the remainder being due to the damage. However, since damage events should outnumber the implanted ions by $\sim 1000:1$, and while this calculation certainly produces an overestimate of the implant contribution, it still suggests that considerable radiation-annealing (or self-annealing) of the damage must occur.

A simple model has been produced for predicting S values in terms of the stress-relieving effects associated with the production of amorphous material. The model has enabled an estimate of the yield stress of the amorphous material to be made. For both Ti^+ and Y^+ implantations comparison with experimental data produces values of this stress-supporting capacity in agreement with known or estimated properties of the amorphous material.

Indentation crack-shortening and suppression was also observed in N^+ and C^+ implanted soda-lime–silica glass samples, suggesting that surface compressive stresses are also generated by similar mechanisms to those proposed for sapphire. The integrated stress values were found to increase with dose, though not with the linear S–dose dependence observed in sapphire. Peak values of integrated stress were found to be $\sim 5 \times 10^{-4}\,\mathrm{MPa\,m}$, and these correspond to stresses of the order of ~ 1 to $2\,\mathrm{GPa}$ being supported within the $\sim 0.3\,\mu\mathrm{m}$ implantation-affected layer. At doses beyond $\sim 5 \times 10^{17}$ ions $\mathrm{cm^{-2}}$, stress relief was observed to occur though the microstructural origin of both this effect and the simple hardening with implantation are unknown.

Acknowledgements

The authors are indebted to Professor D. Hull, and formerly Professor K. W. K. Honeycombe for provision of laboratory facilities and to Drs G. Dearnaley, N. Eyre and A. Saint for the provision of (and technical assistance with) the implantation, Rutherford back-scattering and nuclear reaction analysis. PJB wishes to acknowledge SERC and AERE Harwell for the provision of a CASE award. We are also grateful to Dr M. G. Pitt, GEC Hirst Research Centre, Wembly for the provision of the sapphire specimens. It is a pleasure to thank Dr E. H. Yoeffe for invaluable discussions concerning near-surface stress states.

References

1. P. J. BURNETT and T. F. PAGE, *J. Mater. Sci.* **19** (1984) 845.
2. *Idem*, "Plastic Deformation of Ceramic Materials", edited by R. C. Bradt and R. E. Tressler (Plenum Press, New York, 1984) p. 669.
3. *Idem, Proc. Mater. Res. Soc.* **27** (1984) 401.
4. J. M. WILLIAMS, C. J. McHARGUE and B. R. APPLETON, *Nucl. Inst. Meth.* **209/210** (1983) 317.
5. J. K. COCHRAN, K. O. LEGG and H. F. SULNICK-LEGG, *Proc. Mater. Res. Soc.* **24** (1984) 173.
6. G. B. KREFFT and E. P. EERNISSE, *J. Appl. Phys.* **49** (1978) 2725.
7. N. E. W. HARTLEY, *J. Vac. Sci. Technol.* **12** (1975) 485.
8. E. P. EERNISSE, *J. Appl. Phys.* **45** (1974) 167.
9. B. V. KING, J. C. KELLY and R. L. DALGLISH, *Nucl. Inst. Meth.* **209/210** (1983) 1135.
10. P. J. BURNETT and T. F. PAGE, *J. Mater. Sci.* **19** (1984) 3524.
11. S. G. ROBERTS and T. F. PAGE, "Ion Implantation into Metals", edited by V. Ashworth, W. A. Grant and R. P. M. Proctor (Pergamon, Oxford, 1982) p. 135.
12. B. R. LAWN and E. R. FULLER, *J. Mater. Sci.* **19** (1984) 4061.
13. T. JENSEN, B. R. LAWN, R. L. DALGLISH and J. C. KELLY, *Radiat. Eff.* **28** (1976) 245.
14. G. CARTER and W. A. GRANT, "Ion Implantation of Semiconductors", (Edward Arnold, London, 1976) p. 42.

15. J. LINDWARD, M. SCHARFF and H. E. SCHIØTT, *Matt. Fys. Med. Kgl. Dansk. Vid. Selsk.* **33** (1963) No. 14.
16. J. H. CRAWFORD, *J. Nucl. Mater.* **108/109** (1982) 644.
17. K. B. WINTERBON, P. SIGMUND and J. B. SANDERS, *Matt. Fys. Med. Kgl. Dansk. Vid. Selsk.* **37** (1970) No. 14.
18. I. MANNING and G. P. MUELLER, *Computer Phys. Commun.* **7** (1974) 85.
19. C. WANG, Y. TAO and S. WANG, *J. Non-Cryst. Solids* **52** (1982) 589.
20. P. MAZZOLDI, *Nucl. Inst. Meth.* **209/210** (1983) 1089.
21. G. DECONNINCK, "Introduction to Radioanalytical Physics" (Elsevier, Amsterdam, 1978).
22. M. D. MATTHEWS, Harwell Report AERE-R-10848 (AERE, Harwell, Oxon, 1983).
23. B. R. LAWN and T. R. WILSHAW, *J. Mater. Sci.* **10** (1975) 1049.
24. H. NARAMOTO, C. W. WHITE, J. M. WILLIAMS, C. J. McHARGUE, O. W. HOLLAND, M. M. ABRAHAM and B. R. APPLETON, *J. Appl. Phys.* **54** (1983) 683.
25. C. J. McHARGUE, H. NARAMOTO, B. R. APPLETON, C. W. WHITE and J. M. WILLIAMS, *Proc. Mater. Res. Soc.* **7** (1982) 147.
26. T. E. MITCHELL and A. H. HEUER, *Mater. Sci. Eng.* **28** (1977) 81.
27. D. M. MARSH, *Proc. R. Soc.* **A279** (1964) 420.
28. K. W. PETER, *J. Non-Cryst. Solids* **5** (1970) 103.
29. K. WITMAAK and G. STAUDENMAIER, *J. Nucl. Mater.* **93/94** (1980) 581.
30. M. L. KRONBERG, *J. Amer. Ceram. Soc.* **45** (1962) 274.
31. B. R. LAWN, A. G. EVANS and D. B. MARSHALL, *ibid.* **63** (1980) 574.
32. G. R. ANSTIS, P. CHANTIKUL, B. R. LAWN and D. B. MARSHALL, *ibid.* **64** (1981) 533.
33. P. M. SARGENT and T. F. PAGE, *Proc. Br. Ceram. Soc.* **26** (1978) 209.
34. J. T. CZERNUSZKA and T. F. PAGE, *ibid.* **34** (1984) 145.
35. R. C. WEAST, "Handbook of Chemistry and Physics" (CRC Press, Cleveland, Ohio, 1976).
36. A. J. BOURDILLON, S. J. BULL, P. J. BURNETT and T. F. PAGE, *J. Mater. Sci.* in press.

Received 22 January and accepted 11 February 1985